ACS APPLIED NANO MATERIALS

www.acsanm.org Article

Bimetallic Iron−Cobalt Nanoparticles Coated with Amorphous Carbon for Oxygen Evolution

Xue Bai, Qiang Wang, and Jingqi Guan*

Cite This: *ACS Appl. Nano Mater.* 2021, 4, 12663−12671 Read Online

ABSTRACT: Because of the adjustable electronic structure of bimetallic alloys, they have received much attention in electrocatalytic reactions. However, to date, there is a lack of effective methods to synthesize bimetallic nanoalloys with controllable metal proportions in the active species of the catalysts prepared by a high-temperature annealing method, leading to inferior catalytic activity and difficulty in identifying the active sites. Here, we synthesize iron (Fe)−cobalt (Co)-based nanoparticles coated with a few layers of amorphous carbon shell (<1 nm) and with Co_7Fe_3 alloy as the core by facile pyrolysis of a bimetallic Fe−Co-based tartrate, which exhibits excellent oxygen evolution reaction (OER) activity with a low overpotential of 272 mV at a current density of 10 mA cm^{-2} and good durability in alkaline media. Compared with single-metal Fe/Co tartrate-derived catalysts, a bimetallic Fe−Co tartrate-derived catalyst with $Co_7Fe_3O_x$ active sites shows higher charge-transfer ability and a lower OER barrier (approximately 285 kJ mol^{-1}). For the first time, this work demonstrates that Fe−Co-based tartrate complexes can be used as precursors to construct high-performance bimetallic Fe−Co-based nanocomposite catalysts with controllable active sites for electrocatalytic OER.

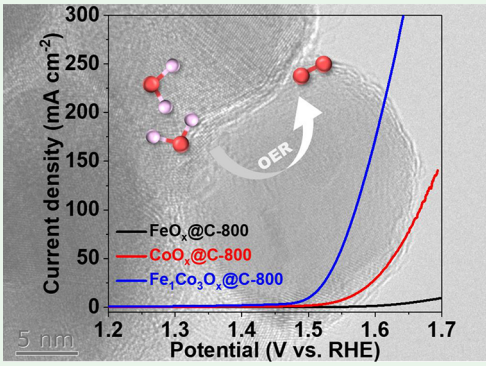

KEYWORDS: *carbonous material, cobalt, iron, oxygen evolution reaction, tartrate*

1. INTRODUCTION

The development of clear and renewable hydrogen energy to replace the traditional fossil fuel is a key to becoming carbon-neutral.[1] Electrochemical water splitting is a clean and effective technique for hydrogen production.[2,3] Currently, large-scale implementation is impeded by the lack of earth-abundant, high-efficiency, and cost-effective transition-metal catalysts to substitute iridium oxide for anodic electrocatalysis of the sluggish oxygen evolution reaction (OER).[4] Thereby, well-stocked catalysts with high OER performance are urgently required to address this predicament.[5]

Transition-metal-based catalysts are active for OER, such as transition-metallic carbides,[6] chalcogenides,[7] nitrides,[8] phosphides,[9] and (oxy)hydroxides.[10] Therein, iron (Fe)-, cobalt (Co)-, and nickel (Ni)-based nanocatalysts have been extensively researched for OER because of their high abundance and relatively low cost.[11] Especially, bimetallic Fe−Co-based and Fe−Ni-based nanocatalysts exhibit enhanced OER activity compared with monometallic counterparts, which are promising candidates used in alkaline electrolysis of water.[12] However, the controllable fabrication of bimetallic electrocatalysts with the uniform dispersion of different metal ions is still challenging.[13] Metal−organic complexes with microporous structures and regulable coordination environments can provide a novel route for constructing metal nanoparticles/carbon nanocomposites by a simple post-treatment.[14] Although Co-based metal−organic frameworks (especially Co-based ZIF-67) have been extensively investigated as precursors to prepare cobalt nanoparticles/carbon nanocomposites,[15] the high price and carcinogenicity of the 2-methylimidazole ligand hindered large-scale application. Tartaric acid (TA) is a nontoxic carboxylic acid that exists in a variety of plants such as grapes and tamarind and has been widely used in the textile printing, dyeing, pharmaceutical, and food industries.[16] Because it possesses two hydroxyl groups and two carboxyl groups in one molecule, TA can coordinate with most of metal ions to form a stable structure. For example, He et al. added L-TA to the mixture of a Co^{2+} and Zn^{2+} solution to form a Co^{2+}/Zn^{2+}−tart complex solution, which was used as the deposition solution to prepare $Zn_xCo_{3-x}O_4$ films by a electrodeposition method.[17] Switzer and co-workers used TA to stabilize Co^{2+} in a strong alkaline solution with pH = 14, which was used as the deposition solution to prepare Co_3O_4 films.[18] Although TA has very strong coordination ability with many metal ions, there are seldom reports about the synthesis of pure ferric tartrate and cobalt tartrate complexes. As far as we are aware, there are no

Received: October 2, 2021
Accepted: October 8, 2021
Published: October 22, 2021

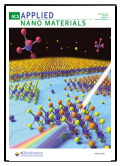

Scheme 1. Illustration of the Fabrication of $Fe_1Co_nO_x$@C-800

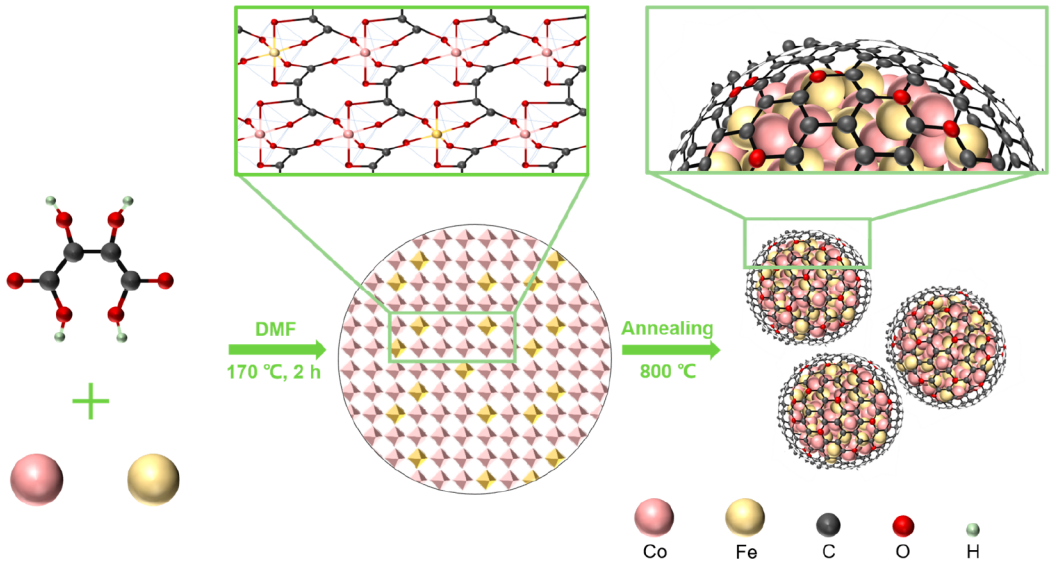

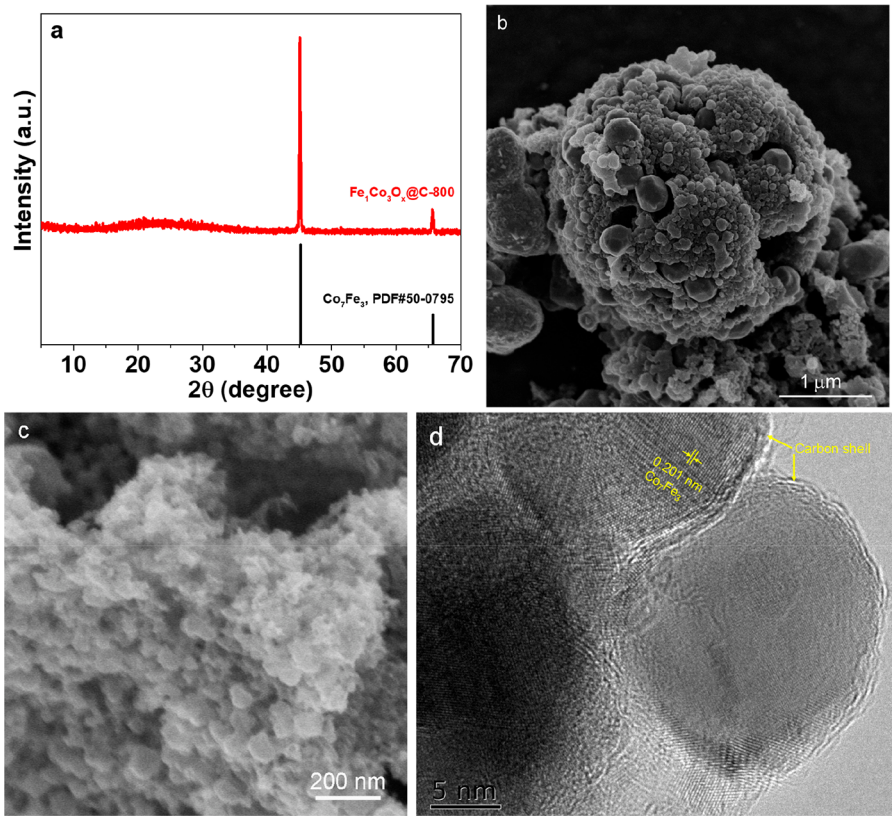

Figure 1. (a) XRD patterns of $Fe_1Co_3O_x$@C-800 and referred sample Co_7Fe_3. (b and c) SEM images of $Fe_1Co_3O_x$@C-800. (d) HRTEM image of $Fe_1Co_3O_x$@C-800.

reports using ferric/cobalt tartrate as precursors to prepare OER electrocatalysts by the pyrolysis method. In addition, although the nitrogen ligand can regulate the electronic structure of metal sites and carbon support, the M−N bonds would be broken under the oxidative environment, resulting in deactivation.[19−25] Therefore, using TA as the ligand to synthesize metal nanoparticles/carbon nanocomposites without nitrogen ligands is more attractive for OER.[26]

Herein, we successfully fabricated a new kind of Fe−Co-based nanocomposite by pyrolysis of bimetallic Fe−Co-based complexes without the nitrogen ligand. The Fe−Co-TAs with different Co/Fe ratios were synthesized by reacting Fe^{3+} and Co^{2+} with TA via a solvothermal method.[27] Then, the Fe−Co-based precursors were annealed at different temperatures under an atmosphere of N_2 to obtain $Fe_1Co_nO_x$@C-*T*, where *n* represents the molar ratio of Co/Fe and *T* represents the annealing temperature. The Co/Fe ratio and annealing temperature were found to play a pivotal role in the production of active Fe_3Co_7 species for OER.

https://doi.org/10.1021/acsanm.1c03208
ACS Appl. Nano Mater. 2021, 4, 12663−12671

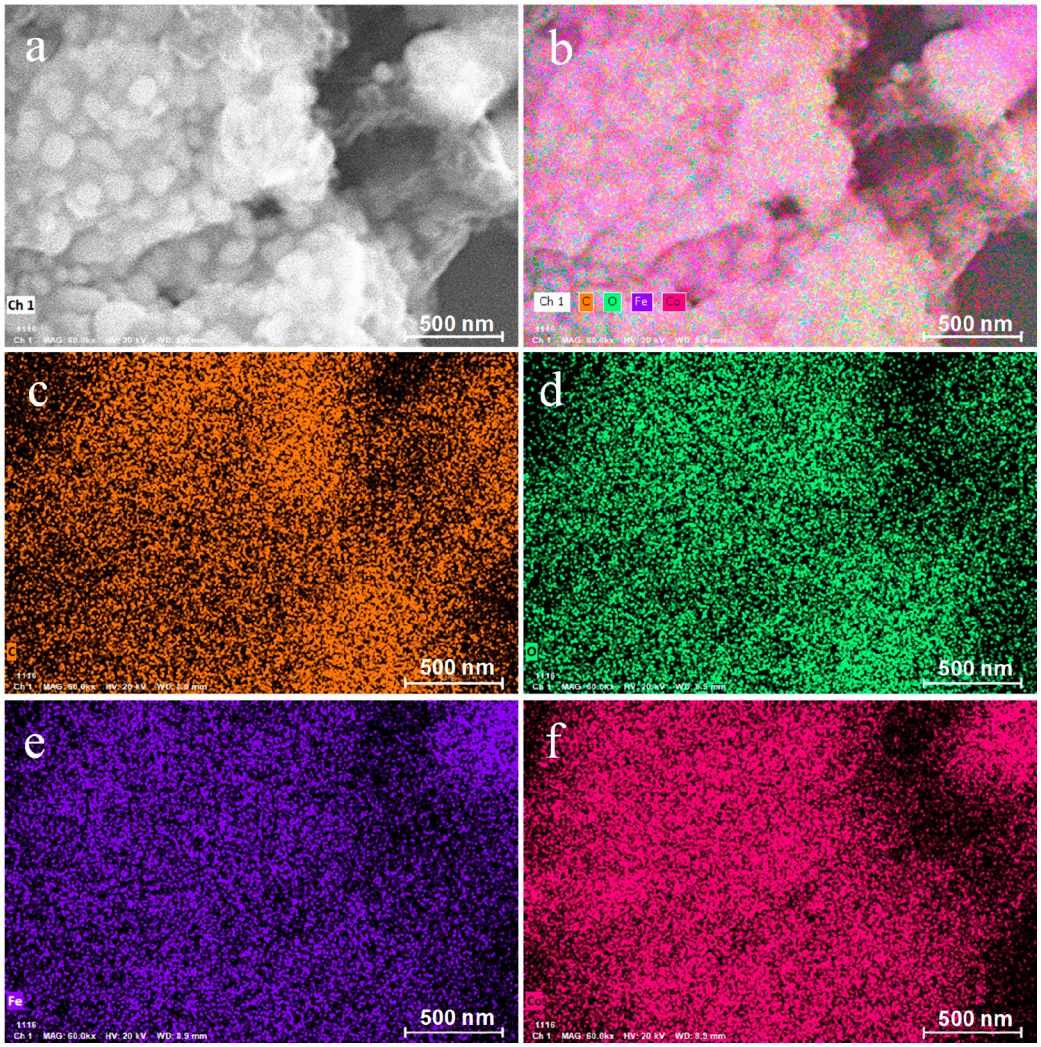

Figure 2. (a) SEM image of $Fe_1Co_3O_x$@C-800 used in the element mapping and (b−f) the corresponding EDS mappings of C, O, Fe, and Co.

2. EXPERIMENTAL SECTION

2.1. Synthesis. *2.1.1. Synthesis of Fe_1Co_n-TA.* Fe_1Co_n-TA was prepared by a solvothermal method. Typically, 0.5 mmol of $FeCl_3 \cdot 6H_2O$, 1.5 mmol of $CoCl_2 \cdot 6H_2O$, and 4.0 mmol of TA were dissolved in 80 mL of *N*,*N*-dimethylformamide, which was poured into a 100 mL Teflon autoclave and heated at 110 °C for 24 h. After filtration, washing with ethanol, and drying, pink crystals were obtained and named Fe_1Co_3-TA. According to the Co/Fe molar ratio, the obtained Fe_1Co_n-TAs were named Fe_1Co_1-TA, Fe_1Co_2-TA, Fe_1Co_3-TA, Fe_1Co_4-TA, and Fe_1Co_5-TA. For comparison, we prepared Fe-TA and Co-TA by a synthetic process similar to that above.

2.1.2. Synthesis of $Fe_1Co_nO_x$@C-T. Fe_1Co_n-TA was annealed in N_2 at different temperatures for 2 h, which was denoted as $Fe_1Co_nO_x$@C-*T* (*T* = 600, 700, 800, and 900 °C). For comparison, Fe-TA and Co-TA were annealed in N_2 at 800 °C for 2 h, which were denoted as FeO_x@C-800 and CoO_x@C-800, respectively.

2.2. Characterization. X-ray diffraction (XRD) patterns were obtained on a Shimadzu XRD-6000 diffractometer using Cu Kα radiation. Infrared spectroscopy was performed on a Nicolet Impact 410 spectrometer. High-resolution transmission electron microscopy (HRTEM) images were obtained on a FEI Tecnai F30 transmission electron microscope. Scanning electron microscopy (SEM) images were obtained on a SU8020 field-emission scanning electron microscope (Hitachi). X-ray photoelectron spectroscopy (XPS) spectra were attained on a Thermo ESCALAB 250Xi.

2.3. Electrochemical Measurements. The electrochemistry tests were carried out on a CHI760E workstation. The electrocatalysts were tested in 1.0 M KOH using a typical three-electrode system. Linear sweep voltammetry (LSV) polarization curves were collected at a scan rate of 5 mV s^{-1} with *iR* compensation. Electrochemical impedance spectroscopy measurements were carried out in the frequency range from 100 kHz to 0.1 Hz with an alternating-current perturbation of 5 mV. The potential was standardized to a reversible hydrogen electrode (RHE) using the formula *E* (vs RHE) = *E* (vs saturated calomel electrode) + 0.241 V + 0.0591pH.

3. RESULTS AND DISCUSSION

The synthetic procedure of Fe_1Co_n-TA and $Fe_1Co_nO_x$@C-800 is illustrated in Scheme 1. The as-synthesized Fe_1Co_n-TA was characterized by XRD and Fourier transform infrared (FTIR). As exhibited in Figure S1, compared with TA, Fe_1Co_n-TA shows different peak positions, indicating different crystal structures. Moreover, with an increase of the Co/Fe ratio, the peak intensity decreases, suggesting a decreased degree of crystallinity. From Figure S2, the FTIR peak positions of Fe_1Co_3-TA show obvious excursions compared with those of TA, implying that Fe/Co ions were successfully coordinated with TA. The structure of $Fe_1Co_3O_x$@C-800 was analyzed by XRD, indicating that the main species in the sample is an alloy with a Co_7Fe_3 component (Figure 1a). However, for $Fe_1Co_1O_x$@C-800, the main species are Fe_3O_4 and Co_1Fe_1, while for $Fe_1Co_2O_x$@C-800 and $Fe_1Co_4O_x$@C-800, Fe_3O_4,

https://doi.org/10.1021/acsanm.1c03208
ACS Appl. Nano Mater. 2021, 4, 12663−12671

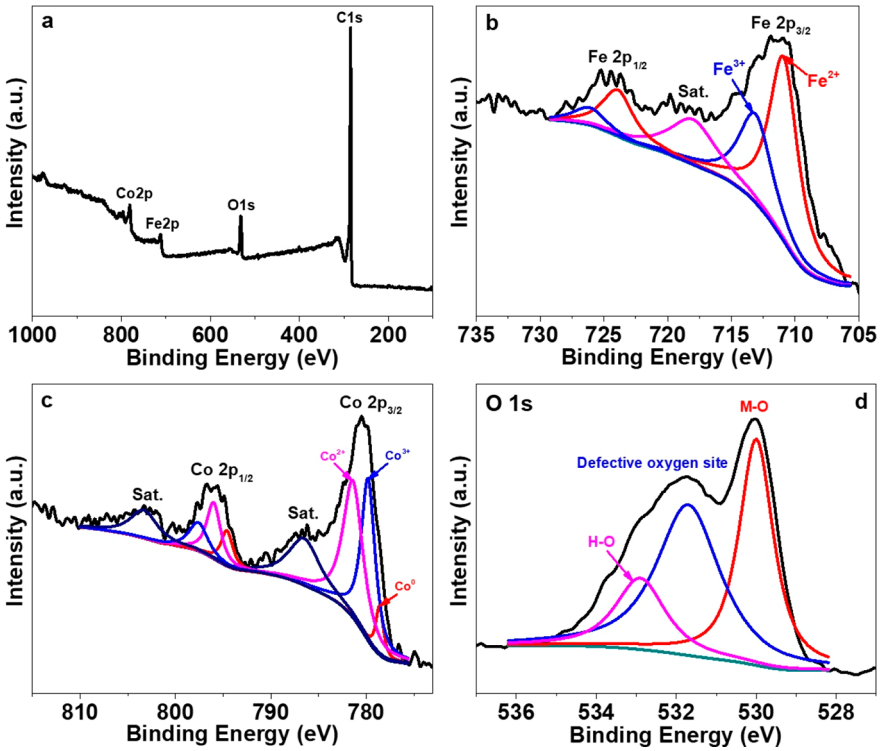

Figure 3. XPS survey spectrum (a) and high-resolution XPS spectra of Fe 2p (b), Co 2p (c), and O 1s (d) of fresh $Fe_1Co_3O_x$@C-800.

Co_1Fe_1, and Co_7Fe_3 coexist (Figure S3). $Fe_1Co_3O_x$@C-800 exhibits a spherical nanostructure involving many small Fe−Co-based nanoparticles (Figure 1b,c), which is similar to those of $Fe_1Co_3O_x$@C-600 and $Fe_1Co_3O_x$@C-700 but different from that of $Fe_1Co_3O_x$@C-900 (Figure S4). For $Fe_1Co_3O_x$@C-900, a typical blocky structure is observed (Figure S4). The average particle size in $Fe_1Co_3O_x$@C-900 is larger than those in $Fe_1Co_3O_x$@C-600, $Fe_1Co_3O_x$@C-700, and $Fe_1Co_3O_x$@C-800. Moreover, the specific surface area reduces with increasing annealing temperature. For instance, the specific surface area of $Fe_1Co_3O_x$@C-600 is 44.3 m^2 g^{-1}, larger than $Fe_1Co_3O_x$@C-700 (40.1 m^2 g^{-1}), $Fe_1Co_3O_x$@C-800 (37.7 m^2 g^{-1}), and $Fe_1Co_3O_x$@C-900 (25.6 m^2 g^{-1}). From the HRTEM image of $Fe_1Co_3O_x$@C-800 (Figure 1d), the lattice distance was measured to be 0.201 nm, corresponding to the (110) crystal face of Co_7Fe_3 (PDF 50-0795) in good agreement with the XRD result. In addition, it can be observed that the Fe−Co-based nanoparticles are wrapped by a few layers (less than 1 nm) of amorphous carbon. The element distribution in $Fe_1Co_3O_x$@C-800 was analyzed on a SEM−energy-dispersive X-ray spectroscopy (EDS) apparatus. As shown in Figure 2, C, O, Fe, and Co are evenly dispersed in the sample.

The surface compositions and chemical valences of Fe/Co were determined by XPS. As exhibited in Figure 3a, the C, O, Fe, and Co elements were detected in $Fe_1Co_3O_x$@C-800. The high-resolution Fe $2p_{3/2}$ peak can be deconvoluted into two peaks at binding energies of 710.9 and 713.1 eV, assigned to Fe^{2+} and Fe^{3+}, respectively (Figure 3b).[28−31] The high-resolution Co $2p_{3/2}$ peak can be fitted into three peaks at 778.6, 779.8, and 781.4 eV, ascribed to Co^0, Co^{3+}, and Co^{2+}, respectively (Figure 3c).[26,32] The high-resolution O 1s peak can be convoluted into three peaks at 530.0, 531.7, and 532.9 eV, attributed to M−O (M = Fe and Co), defective oxygen sites, and hydroxyl groups, respectively (Figure 3d).[33−36]

The OER properties of the TA-derived catalysts were investigated by LSV. As displayed in Figure 4a, FeO_x@C-800 shows poor OER activity with a high overpotential (η_{10}) of 476 mV at a current density of 10 mA cm^{-2}, which is much larger than that (331 mV) achieved on CoO_x@C-800. Bimetallic $Fe_1Co_3O_x$@C-800 exhibits an η_{10} value of 272 mV, smaller than those achieved on the monometallic Fe−Co-TA-derived catalysts and most previously reported Fe−Co-based electrocatalysts (Table 1). The Tafel slope on $Fe_1Co_3O_x$@C-800 is 40 mV $decade^{-1}$, far lower than those for FeO_x@C-800 (150 mV $decade^{-1}$) and CoO_x@C-800 (74 mV $decade^{-1}$), suggesting favorable OER kinetics and the second electron transfer as the potential-determining step on $Fe_1Co_3O_x$@C-800.[37] Thereby, the introduction of Fe ions promotes OER electrocatalysis in accordance with previous findings.[28,38] The OER energy barrier (ΔG) on FeO_x@C-800, CoO_x@C-800, and $Fe_1Co_3O_x$@C-800 can be determined from eqs 1−3.[39]

$$j = j_0[-e^{-\alpha nF(E-E_0)/RT} + e^{(1-\alpha)nF(E-E_0)/RT}] \quad (1)$$

$$\Delta G = (1-\alpha)nFE_0 - (1-\alpha)nFE \quad (2)$$

$$1-\alpha = \frac{1}{1+\frac{-k_1}{k_2}} \quad (3)$$

where T is the temperature, R is the gas constant (8.314 J mol^{-1} k^{-1}), n is the electron-transfer number (n = 4), F is the Faraday constant (96485 C mol^{-1}), J_0 is the exchange current density, and k_1 and k_2 are the cathodic and anodic Tafel slopes, respectively. When the applied potential (E) is 0 V, ΔG is calculated to be approximately 392, 374, and 285 kJ mol^{-1} for FeO_x@C-800, CoO_x@C-800, and $Fe_1Co_3O_x$@C-800, respectively, indicating lower reaction barriers on bimetallic $Fe_1Co_3O_x$@C-800 than on monometallic FeO_x@C-800 and CoO_x@C-800.

https://doi.org/10.1021/acsanm.1c03208
ACS Appl. Nano Mater. 2021, 4, 12663−12671

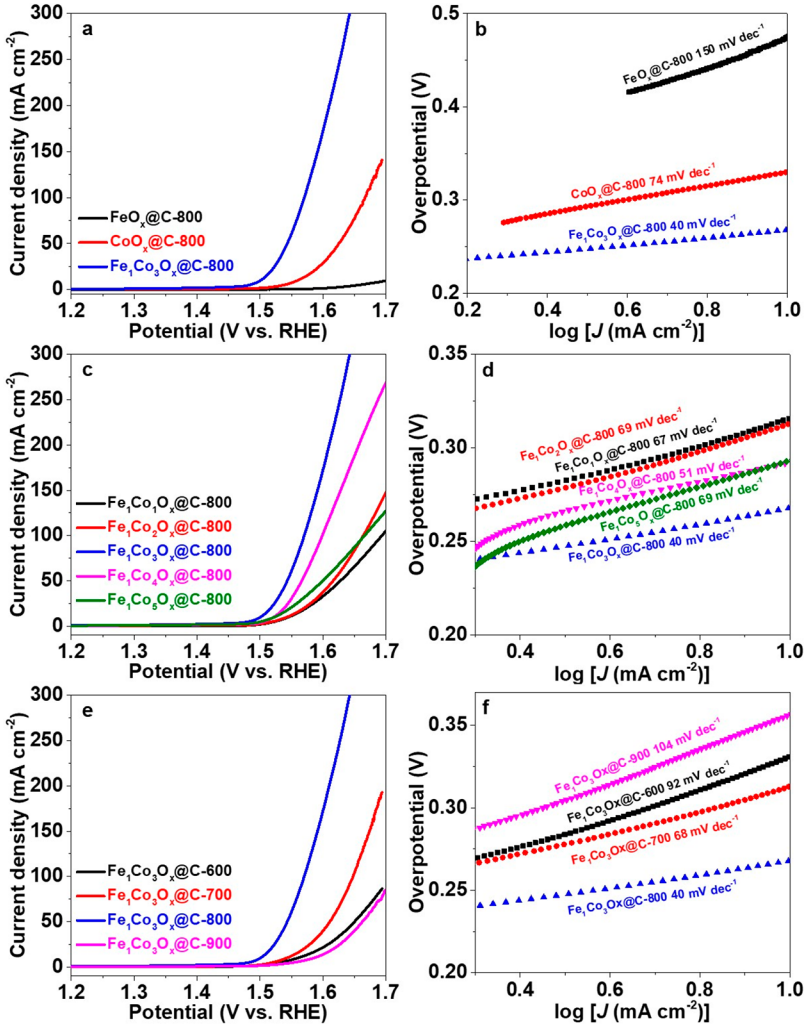

Figure 4. LSV curves of (a) FeO_x@C-800, CoO_x@C-800, and $Fe_1Co_3O_x$@C-800, (c) $Fe_1Co_nO_x$@C-800 with different Co/Fe ratios, and (d) $Fe_1Co_3O_x$@C-*T* annealed at different temperatures. (b, d, and f) Tafel plots.

Because Fe plays a positive role in accelerating OER activity, the influence of the Co/Fe molar ratios in the bimetallic TA-derived catalysts on the electrocatalytic performance was investigated. As illustrated in Figure 4c, $Fe_1Co_3O_x$@C-800 with Co:Fe = 3:1 shows a lower overpotential (η_{10}) than $Fe_1Co_1O_x$@C-800 (317 mV), $Fe_1Co_2O_x$@C-800 (314 mV), $Fe_1Co_4O_x$@C-800 (293 mV), and $Fe_1Co_5O_x$@C-800 (294 mV). Moreover, all of the $Fe_1Co_nO_x$@C-800 samples show lower OER overpotentials than FeO_x@C-800 and CoO_x@C-800, further indicating the synergetic effect between Fe and Co. However, the Tafel slopes for $Fe_1Co_1O_x$@C-800, $Fe_1Co_2O_x$@C-800, and $Fe_1Co_5O_x$@C-800 are close to 69 mV decade^{-1}, slightly lower than that for CoO_x@C-800 (74 mV decade^{-1}), implying that the OER rate-determining step might be followed by the first electron transfer (Figure 4d).[60] From XRD analysis, Fe_3O_4 and Co_1Fe_1 alloy are the main species in the $Fe_1Co_1O_x$@C-800 sample, while the Co_3Fe_1 species is absent. With increasing Co/Fe ratio in the sample, the Co_3Fe_1 species is gradually formed and the relative content reaches a maximum in the $Fe_1Co_3O_x$@C-800 sample. Further increasing the Co/Fe ratio would lead to the formation of other species, such as Fe_3O_4 and Co_1Fe_1 alloy. Considering that the OER activity of $Fe_1Co_1O_x$@C-800 is the lowest among the $Fe_1Co_nO_x$@C-800 samples and the OER activity of FeO_x@C-800 is very poor, it is reasonable to infer that the intrinsic activity of Fe_3O_4 and Co_1Fe_1 is inferior to that of the Co_3Fe_1 species for the OER. As a result, the $Fe_1Co_1O_x$@C-800 sample with the highest content of Co_3Fe_1 species exhibits the best OER performance among the $Fe_1Co_nO_x$@C-800 samples.

The effect of the pyrolysis temperature on the OER performance of $Fe_1Co_3O_x$@C-*T* was researched. As depicted in Figure 4e, $Fe_1Co_3O_x$@C-800 exhibits lower overpotential (η_{10}) than $Fe_1Co_3O_x$@C-600 (332 mV), $Fe_1Co_3O_x$@C-700 (314 mV), and $Fe_1Co_3O_x$@C-900 (357 mV). The better OER performance of $Fe_1Co_3O_x$@C-800 can be further reflected by its smaller Tafel slope than those of $Fe_1Co_3O_x$@C-600 (92 mV decade^{-1}), $Fe_1Co_3O_x$@C-700 (68 mV decade^{-1}), and $Fe_1Co_3O_x$@C-900 (104 mV decade^{-1}) (Figure 4f). To explore the influence of the annealing temperature on the OER performance, we performed XRD analysis. As discussed above, the Co_7Fe_3 alloy is the main species in $Fe_1Co_3O_x$@C-800, while Co_7Fe_3 and CoFe alloys coexist in $Fe_1Co_3O_x$@C-700 and the CoFe alloy is the main species in $Fe_1Co_3O_x$@C-900 (Figure S5). Combined with the electrocatalytic performance and aforementioned results, it can be further verified that catalysts with Co_7Fe_3 species exhibit higher OER activity than those with Co_1Fe_1 species. In addition, we measured the electrochemical surface area of $Fe_1Co_3O_x$@C-*T* to further

https://doi.org/10.1021/acsanm.1c03208
ACS Appl. Nano Mater. 2021, 4, 12663−12671

Table 1. Comparison of the OER Performances of Fe−Co-Based Electrocatalysts

catalyst	electrolyte	overpotential (mV) at 10 mA cm^{-2}	ref
$Fe_1Co_3O_x$@C-800	1.0 M KOH	272	this work
$Co_{0.17}Fe_{0.79}P$/NC	1.0 M KOH	299	40
$LaCoO_{3-\delta}$	0.1 M KOH	330	41
BC/Co_3O_4	1.0 M KOH	310	42
$Fe(OH)_3$@Co-MOF-74	1.0 M KOH	292	43
Fe_2O_3@Ni-MOF-74	1.0 M KOH	264	44
NGO/Ni_7S_6	0.1 M KOH	380	45
porous Ni_2P nanosheets	1.0 M KOH	320	46
BMM-11	1.0 M KOH	362	47
$[Co(L1)(HL3)_2\cdot(H_2O)_2]_n$	1.0 M KOH	398	48
M-PCBN/CC	1.0 M KOH	348	49
$Co_{2.36}Fe_{0.19}Ni_{0.45}$-btca	1.0 M KOH	292	50
Co@NPC	1.0 M NaOH	540	51
PB-Co/Co−NPHCS	0.1 M KOH	370	52
TMOF-4 nanosheets	1.0 M KOH	318	53
UTSA-16	1.0 M KOH	408	54
Co/W−C@NCNSs	1.0 M KOH	323	55
SnO_2 and CTGU-14	0.1 M KOH	388	56
Co-MONs	1.0 M KOH	309	57
$CoSe_2$	1.0 M KOH	330	58
Co_2P@C	1.0 M KOH	328	59

reveal the number of electrochemical active sites for the OER. As demonstrated in Figures S6−S9, the electrochemical active surface areas for $Fe_1Co_3O_x$@C-600, $Fe_1Co_3O_x$@C-700, $Fe_1Co_3O_x$@C-800, and $Fe_1Co_3O_x$@C-900 are 157, 561, 592, and 477 cm^2, respectively, indicating that $Fe_1Co_3O_x$@C-800 possesses more electrocatalytic active sites than $Fe_1Co_3O_x$@C-600, $Fe_1Co_3O_x$@C-700, and $Fe_1Co_3O_x$@C-900. Considering that the specific surface area decreases with increasing annealing temperature and $Fe_1Co_3O_x$@C-800 shows a smaller surface area than $Fe_1Co_3O_x$@C-600 and $Fe_1Co_3O_x$@C-700, the increased active sites should be ascribed to the more efficient OER performance of the Co_7Fe_3 species than Fe_3O_4 and Co_1Fe_1 alloy. The enhanced OER activity of the Co_7Fe_3 species is attributed to a cooperation mechanism between Fe and Co ions, which can be evidenced by the CV curves (Figure S10). CoO_x@C-800 shows a reversible wave at $E_{1/2}$ = ca. 1.43 V due to the redox reaction of a Co^{II}/Co^{III} couple, which disappears when Fe ions were introduced, implying that there is a strong electronic interaction between Co and Fe.[61] Many studies have shown that the introduction of a small amount of Fe into Co-based systems can promote the OER activity. For instance, Wang et al. found that α-$Co_4Fe(OH)_x$ nanoplates exhibited lower OER overpotential than α-$Co(OH)_2$ because cooperation between Fe and Co will affect the adsorption of O and OH, thus increasing their Gibbs free energy difference.[61] Hu et al. found that the addition of Fe^{3+} into the electrolyte can accelerate the OER of an atomic Co−N−C catalyst.[38] Using operando X-ray absorption spectroscopy, they revealed that the formation of Co−O−Fe active sites facilitated the OER process. In addition, compared with carbon supports, the electronic states around the Fermi level were increased in FeCo alloy nanoparticles encapsulated by carbon, thus improving the OER activity.[62] Our calculation results demonstrate that $Fe_1Co_3O_x$@C-800 exhibits a much lower OER energy barrier than FeO_x@C-800 and CoO_x@C-800, implying that Fe and Co are involved in the electrocatalytic water oxidation process. Furthermore, we have measured the charge-transfer resistance (R_{ct}) of $Fe_1Co_3O_x$@C-T to uncover the charge-transfer ability. As exhibited in Figure S11, $Fe_1Co_3O_x$@C-800 shows a low R_{ct} of 15.6 Ω cm^2, smaller than those for $Fe_1Co_3O_x$@C-600 (32.2 Ω cm^2), $Fe_1Co_3O_x$@C-700 (16.2 Ω cm^2), and $Fe_1Co_3O_x$@C-900 (30.5 Ω cm^2), suggesting better charge-transfer ability and more favorable OER kinetics on the former.

The durability of $Fe_1Co_3O_x$@C-800 for OER was evaluated by chronopotentiometry measurement. As revealed in Figure S12, after continuous operation for 12 h, the potential increased by only 5 mV, which might be due to the resulting oxygen bubbles and partial shedding of the catalyst from the glassy carbon electrode. The structure of $Fe_1Co_3O_x$@C-800 after the OER stability test was characterized by XRD. As demonstrated in Figure S13, the peaks due to the Co_7Fe_3 alloy can be obviously observed, implying that the structure of $Fe_1Co_3O_x$@C-800 after OER electrocatalysis is well maintained because of protection of the carbon shells from oxidation during OER. The surface composites and metal valence states in $Fe_1Co_3O_x$@C-800 after OER electrocatalysis were identified by XPS. As shown in Figure 5, the Fe and Co elements can be obviously detected on the catalyst surface. The surface Fe^{3+}/Fe^{2+} ratio increased from 0.55:1 in the fresh sample to 1:1 in the used one, indicating that partial Fe^{2+} was oxidized to Fe^{3+} after OER. Moreover, the surface Co^0 was completely oxidized to higher valence states, and the peak area of Co^{2+} from the sample after OER increased, suggesting that the unprotected surface Co^0 was oxidized to Co^{2+}. Furthermore, the relative content of defective oxygen sites increased after OER electrocatalysis, implying that surface −OH species took part in the reaction and defect sites were generated. Therefore, partially exposed Fe−CoO_x should be the active species for OER, while the carbon-coated Fe−Co-based nanoalloy promotes charge transfer and OER kinetics. The XPS results indicate that Fe and Co are involved in the water oxidation process, which might undergo Fe^{2+} (e.g., $Fe(OH)_2$) → Fe^{3+} (e.g., FeOOH) → Fe^{4+} and Co^{2+} (e.g., $Co(OH)_2$) → Co^{3+} (e.g., CoOOH) → Co^{4+}, in agreement with previous reports.[63−65]

4. CONCLUSIONS

In conclusion, we have demonstrated that bimetallic Fe−Co nanoparticles with uniform dispersion of Fe−Co species coated by amorphous carbon can be synthesized by a simple pyrolysis of Fe−Co-based complexes. The Co−Fe content and pyrolysis temperature would influence the components of Fe−Co-TA-derived catalysts. $Fe_1Co_3O_x$@C-800 with a Co_7Fe_3

https://doi.org/10.1021/acsanm.1c03208
ACS Appl. Nano Mater. 2021, 4, 12663−12671

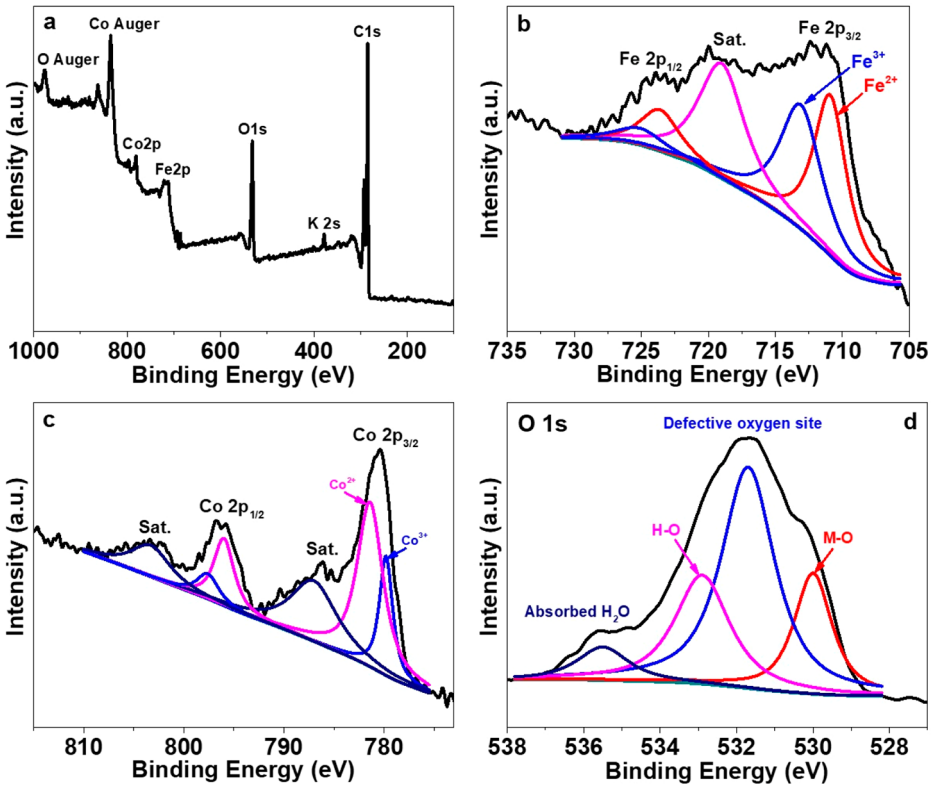

Figure 5. XPS survey spectrum (a) and high-resolution XPS spectra of Fe 2p (b), Co 2p (c), and O 1s (d) of the used $Fe_1Co_3O_x$@C-800 after the OER stability test.

alloy as the main component showed higher electrocatalytic OER activity than those with a CoFe alloy as the main component because of a better charge-transfer ability and smaller OER energy barrier. This work could provide helpful inspiration to the fabrication of bimetallic OER electrocatalysts using TA complexes as precursors via a simple pyrolysis method.

■ ASSOCIATED CONTENT

Supporting Information

The Supporting Information is available free of charge at https://pubs.acs.org/doi/10.1021/acsanm.1c03208.

Additional XRD patterns, FTIR spectra, SEM images, CV curves, Nyquist plots, and a chronopotentiometry curve (PDF)

■ AUTHOR INFORMATION

Corresponding Author

Jingqi Guan − *Institute of Physical Chemistry, College of Chemistry, Jilin University, Changchun 130021, P. R. China;* orcid.org/0000-0002-8498-1963; Email: guanjq@jlu.edu.cn

Authors

Xue Bai − *Institute of Physical Chemistry, College of Chemistry, Jilin University, Changchun 130021, P. R. China*

Qiang Wang − *Institute of Physical Chemistry, College of Chemistry, Jilin University, Changchun 130021, P. R. China*

Complete contact information is available at: https://pubs.acs.org/10.1021/acsanm.1c03208

Notes

The authors declare no competing financial interest.

■ ACKNOWLEDGMENTS

This work was supported by the National Natural Science Foundation of China (Grant 22075099) and the Natural Science Foundation of Jilin Province (Grant 20180101291JC).

■ REFERENCES

(1) Radwan, A.; Jin, H.; He, D.; Mu, S. Design engineering, synthesis protocols, and energy applications of MOF-derived electrocatalysts. *Nano-Micro Lett.* **2021**, *13*, 132.

(2) Zhang, X.-P.; Wang, H.-Y.; Zheng, H.; Zhang, W.; Cao, R. O-O bond formation mechanisms during the oxygen evolution reaction over synthetic molecular catalysts. *Chin. J. Catal.* **2021**, *42*, 1253−1268.

(3) Li, Z.; Hu, M.; Wang, P.; Liu, J.; Yao, J.; Li, C. Heterojunction catalyst in electrocatalytic water splitting. *Coord. Chem. Rev.* **2021**, *439*, 213953.

(4) Yan, Y.; Wang, P.; Lin, J.; Cao, J.; Qi, J. Modification strategies on transition metal-based electrocatalysts for efficient water splitting. *J. Energy Chem.* **2021**, *58*, 446−462.

(5) Wang, J.; Xu, F.; Jin, H.; Chen, Y.; Wang, Y. Non-Noble Metal-based Carbon Composites in Hydrogen Evolution Reaction: Fundamentals to Applications. *Adv. Mater.* **2017**, *29*, 1605838.

(6) Huang, H.; Kong, L.; Liu, M.; He, J.; Shuang, W.; Xu, Y.; Bu, X.-H. Constructing bifunctional Co/MoC@N-C catalyst via an in-situ encapsulation strategy for efficient oxygen electrocatalysis. *J. Energy Chem.* **2021**, *59*, 538−546.

(7) Huang, J.; Wang, S.; Nie, J.; Huang, C.; Zhang, X.; Wang, B.; Tang, J.; Du, C.; Liu, Z.; Chen, J. Active site and intermediate modulation of 3D CoSe2 nanosheet array on Ni foam by Mo doping for high-efficiency overall water splitting in alkaline media. *Chem. Eng. J.* **2021**, *417*, 128055.

(8) Qin, R.; Wang, P.; Lin, C.; Cao, F.; Zhang, J.; Chen, L.; Mu, S. Transition Metal Nitrides: Activity Origin, Synthesis and Electrocatalytic Applications. *Wuli Huaxue Xuebao* **2020**, *37*, 2009099.
(9) Wu, L.; Yu, L.; McElhenny, B.; Xing, X.; Luo, D.; Zhang, F.; Bao, J.; Chen, S.; Ren, Z. Rational design of core-shell-structured CoPx@FeOOH for efficient seawater electrolysis. *Appl. Catal., B* **2021**, *294*, 120256.
(10) Zhang, B.; Zheng, X.; Voznyy, O.; Comin, R.; Bajdich, M.; García-Melchor, M.; Han, L.; Xu, J.; Liu, M.; Zheng, L.; García de Arquer, F. P.; Dinh, C. T.; Fan, F.; Yuan, M.; Yassitepe, E.; Chen, N.; Regier, T.; Liu, P.; Li, Y.; De Luna, P.; Janmohamed, A.; Xin, H. L.; Yang, H.; Vojvodic, A.; Sargent, E. H. Homogeneously dispersed multimetal oxygen-evolving catalysts. *Science* **2016**, *352*, 333−337.
(11) Hisai, Y.; Ma, Q.; Qureishy, T.; Watanabe, T.; Higo, T.; Norby, T.; Sekine, Y. Enhanced activity of catalysts on substrates with surface protonic current in an electrical field - a review. *Chem. Commun.* **2021**, *57*, 5737−5749.
(12) Liang, Q.; Chen, J.; Wang, F.; Li, Y. Transition metal-based metal-organic frameworks for oxygen evolution reaction. *Coord. Chem. Rev.* **2020**, *424*, 213488.
(13) Zheng, S.; Li, X.; Yan, B.; Hu, Q.; Xu, Y.; Xiao, X.; Xue, H.; Pang, H. Transition-Metal (Fe, Co, Ni) Based Metal-Organic Frameworks for Electrochemical Energy Storage. *Adv. Energy Mater.* **2017**, *7*, 1602733.
(14) Wen, X.; Zhang, Q.; Guan, J. Applications of metal−organic framework-derived materials in fuel cells and metal-air batteries. *Coord. Chem. Rev.* **2020**, *409*, 213214.
(15) Li, S.; Gao, Y.; Li, N.; Ge, L.; Bu, X.; Feng, P. Transition metal-based bimetallic MOFs and MOF-derived catalysts for electrochemical oxygen evolution reaction. *Energy Environ. Sci.* **2021**, *14*, 1897−1927.
(16) Garcia, A. C.; Sanchez-Martinez, C.; Bakker, I.; Goetheer, E. Sustainable electrochemical production of tartaric acid. *ACS Sustainable Chem. Eng.* **2020**, *8*, 10454−10460.
(17) Han, S.; Liu, S.; Wang, R.; Liu, X.; Bai, L.; He, Z. One-Step ElectrodepositiOn of Nanocrystalline ZnxCo3-xO4 Films with High Activity and Stability for Electrocatalytic Oxygen Evolution. *ACS Appl. Mater. Interfaces* **2017**, *9*, 17186−17194.
(18) Koza, J. A.; He, Z.; Miller, A. S.; Switzer, J. A. Electrodeposition of Crystalline Co3O4-A Catalyst for the Oxygen Evolution Reaction. *Chem. Mater.* **2012**, *24*, 3567−3573.
(19) Chen, C.; Tuo, Y.; Lu, Q.; Lu, H.; Zhang, S.; Zhou, Y.; Zhang, J.; Liu, Z.; Kang, Z.; Feng, X.; Chen, D. Hierarchical trimetallic Co-Ni-Fe oxides derived from core-shell structured metal-organic frameworks for highly efficient oxygen evolution reaction. *Appl. Catal., B* **2021**, *287*, 119953.
(20) Duan, X.; Ren, S.; Pan, N.; Zhang, M.; Zheng, H. MOF-derived Fe,Co@N-C bifunctional oxygen electrocatalysts for Zn-air batteries. *J. Mater. Chem. A* **2020**, *8*, 9355−9363.
(21) Hong, W.; Kitta, M.; Xu, Q. Bimetallic MOF-Derived FeCo-P/C Nanocomposites as Efficient Catalysts for Oxygen Evolution Reaction. *Small Methods* **2018**, *2*, 1800214.
(22) Wang, P.; Xu, Z.; Lin, Y.; Wan, L.; Wang, B. Exceptional Performance of MOF-Derived N-Doped CoP and Fe-Doped CoOOH Ultrathin Nanosheets Electrocatalysts for Overall Water Splitting. *ACS Sustainable Chem. Eng.* **2020**, *8*, 8949−8957.
(23) Wu, M.; Hu, X.; Li, C.; Li, J.; Zhou, H.; Zhang, X.; Liu, R. Encapsulation of metal precursor within ZIFs for bimetallic N-doped carbon electrocatalyst with enhanced oxygen reduction. *Int. J. Hydrogen Energy* **2018**, *43*, 14701−14709.
(24) Yuan, Q.; Yu, Y.; Sherrell, P. C.; Chen, J.; Bi, X. Fe/Co-based Bimetallic MOF-derived Co3Fe7@NCNTFs Bifunctional Electrocatalyst for High-Efficiency Overall Water Splitting. *Chem. - Asian J.* **2020**, *15*, 1728−1735.
(25) Ren, Q.; Wang, H.; Lu, X.-F.; Tong, Y.-X.; Li, G.-R. Recent Progress on MOF-Derived Heteroatom-Doped Carbon-Based Electrocatalysts for Oxygen Reduction Reaction. *Adv. Sci.* **2018**, *5*, 1700515.
(26) Li, M.; Bai, L.; Wu, S.; Wen, X.; Guan, J. Co/CoOx Nanoparticles Embedded on Carbon for Efficient Catalysis of Oxygen Evolution and Oxygen Reduction Reactions. *ChemSusChem* **2018**, *11*, 1722−1727.
(27) Jiang, Z.-G.; Lv, Y.-K.; Cheng, J.-W.; Feng, Y.-L. Two types of rare earth−organic frameworks constructed by racemic tartaric acid. *J. Solid State Chem.* **2012**, *185*, 253−263.
(28) Jin, H.; Mao, S.; Zhan, G.; Xu, F.; Bao, X.; Wang, Y. Fe incorporated alpha-Co(OH)(2) nanosheets with remarkably improved activity towards the oxygen evolution reaction. *J. Mater. Chem. A* **2017**, *5*, 1078−1084.
(29) Yang, J.; Wang, X.; Li, B.; Ma, L.; Shi, L.; Xiong, Y.; Xu, H. Novel iron/cobalt-containing polypyrrole hydrogel-derived trifunctional electrocatalyst for self-powered overall water splitting. *Adv. Funct. Mater.* **2017**, *27*, 1606497.
(30) Wu, Z.; Wang, X.; Huang, J.; Gao, F. A Co-doped Ni-Fe mixed oxide mesoporous nanosheet array with low overpotential and high stability towards overall water splitting. *J. Mater. Chem. A* **2018**, *6*, 167−178.
(31) Wang, A.-L.; Xu, H.; Li, G.-R. NiCoFe layered triple hydroxides with porous structures as high-performance electrocatalysts for overall water splitting. *ACS Energy Lett.* **2016**, *1*, 445−453.
(32) Wan, S.; Qi, J.; Zhang, W.; Wang, W.; Zhang, S.; Liu, K.; Zheng, H.; Sun, J.; Wang, S.; Cao, R. Hierarchical Co(OH)F Superstructure Built by Low-Dimensional Substructures for Electrocatalytic Water Oxidation. *Adv. Mater.* **2017**, *29*, 1700286.
(33) Dong, C.; Yuan, X.; Wang, X.; Liu, X.; Dong, W.; Wang, R.; Duan, Y.; Huang, F. Rational design of cobalt-chromium layered double hydroxide as a highly efficient electrocatalyst for water oxidation. *J. Mater. Chem. A* **2016**, *4*, 11292−11298.
(34) Zhang, Q.; Liu, N.; Guan, J. Charge-transfer effects in Fe-Co and Fe-Co-Y oxides for electrocatalytic water oxidation reaction. *ACS Appl. Energy Mater.* **2019**, *2*, 8903−8911.
(35) Liu, N.; Guan, J. Core−shell Co3O4@ FeOx catalysts for efficient oxygen evolution reaction. *Mater. Today Energy* **2021**, *21*, 100715.
(36) Li, Y.; Lu, M.; Wu, Y.; Ji, Q.; Xu, H.; Gao, J.; Qian, G.; Zhang, Q. Morphology regulation of metal-organic framework-derived nanostructures for efficient oxygen evolution electrocatalysis. *J. Mater. Chem. A* **2020**, *8*, 18215−18219.
(37) Shi, Y.; Zhang, B. Recent advances in transition metal phosphide nanomaterials: synthesis and applications in hydrogen evolution reaction. *Chem. Soc. Rev.* **2016**, *45*, 1529−1541.
(38) Bai, L.; Hsu, C.-S.; Alexander, D.; Chen, H. M.; Hu, X. A cobalt-iron double-atom catalyst for the oxygen evolution reaction. *J. Am. Chem. Soc.* **2019**, *141*, 14190−14199.
(39) Liu, N.; Zhang, Q.; Guan, J. A binuclear Co-based metal-organic framework towards efficient oxygen evolution reaction. *Chem. Commun.* **2021**, *57*, 5016−5019.
(40) Chen, J.; Zhang, Y.; Ye, H.; Xie, J.-Q.; Li, Y.; Yan, C.; Sun, R.; Wong, C.-P. Metal−Organic Framework-Derived $Co_xFe_{1-x}P$ Nanoparticles Encapsulated in N-Doped Carbon as Efficient Bifunctional Electrocatalysts for Overall Water Splitting. *ACS Appl. Energy Mater.* **2019**, *2*, 2734−2742.
(41) Wang, X.; Ge, L.; Lu, Q.; Dai, J.; Guan, D.; Ran, R.; Weng, S.-C.; Hu, Z.; Zhou, W.; Shao, Z. High-performance metal-organic framework-perovskite hybrid as an important component of the air-electrode for rechargeable Zn-Air battery. *J. Power Sources* **2020**, *468*, 228377.
(42) Zou, L.; Xu, Q. Synthesis of a Hierarchically Porous C/Co_3O_4 Nanostructure with Boron Doping for Oxygen Evolution Reaction. *Chem. - Asian J.* **2020**, *15*, 490−493.
(43) Gao, Z.; Yu, Z. W.; Liu, F. Q.; Yang, C.; Yuan, Y. H.; Yu, Y.; Luo, F. Stable Iron Hydroxide Nanosheets@Cobalt-Metal-Organic-Framework Heterostructure for Efficient Electrocatalytic Oxygen Evolution. *ChemSusChem* **2019**, *12*, 4623−4628.
(44) Gao, Z.; Yu, Z. W.; Liu, F. Q.; Yu, Y.; Su, X. M.; Wang, L.; Xu, Z. Z.; Yang, Y. L.; Wu, G. R.; Feng, X. F.; Luo, F. Ultralow-Content Iron-Decorated Ni-MOF-74 Fabricated by a Metal-Organic Frame-

https://doi.org/10.1021/acsanm.1c03208
ACS Appl. Nano Mater. 2021, 4, 12663−12671

work Surface Reaction for Efficient Electrocatalytic Water Oxidation. *Inorg. Chem.* **2019**, *58*, 11500−11507.
(45) Jayaramulu, K.; Masa, J.; Tomanec, O.; Peeters, D.; Ranc, V.; Schneemann, A.; Zboril, R.; Schuhmann, W.; Fischer, R. A. Nanoporous Nitrogen-Doped Graphene Oxide/Nickel Sulfide Composite Sheets Derived from a Metal-Organic Framework as an Efficient Electrocatalyst for Hydrogen and Oxygen Evolution. *Adv. Funct. Mater.* **2017**, *27*, 1700451.
(46) Wang, Q.; Liu, Z.; Zhao, H.; Huang, H.; Jiao, H.; Du, Y. MOF-derived porous Ni2P nanosheets as novel bifunctional electrocatalysts for the hydrogen and oxygen evolution reactions. *J. Mater. Chem. A* **2018**, *6*, 18720−18727.
(47) Zhong, L.; Ding, J.; Wang, X.; Chai, L.; Li, T. T.; Su, K.; Hu, Y.; Qian, J.; Huang, S. Structural and Morphological Conversion between Two Co-Based MOFs for Enhanced Water Oxidation. *Inorg. Chem.* **2020**, *59*, 2701−2710.
(48) Han, D.; Huang, K.; Li, X.; Peng, M.; Jing, L.; Yu, B.; Chen, Z.; Qin, D. Temperature-induced structural diversity of metal−organic frameworks and their applications in selective sensing of nitrobenzene and electrocatalyzing the oxygen evolution reaction. *RSC Adv.* **2019**, *9*, 33890−33897.
(49) Zhang, W.; Wang, Y.; Zheng, H.; Li, R.; Tang, Y.; Li, B.; Zhu, C.; You, L.; Gao, M. R.; Liu, Z.; Yu, S. H.; Zhou, K. Embedding Ultrafine Metal Oxide Nanoparticles in Monolayered Metal-Organic Framework Nanosheets Enables Efficient Electrocatalytic Oxygen Evolution. *ACS Nano* **2020**, *14*, 1971−1981.
(50) Yuan, J. T.; Hou, J. J.; Liu, X. L.; Feng, Y. R.; Zhang, X. M. Optimized trimetallic benzotriazole-5-carboxylate MOFs with coordinately unsaturated active sites as an efficient electrocatalyst for the oxygen evolution reaction. *Dalton Trans* **2020**, *49*, 750−756.
(51) Nath, K.; Bhunia, K.; Pradhan, D.; Biradha, K. MOF-templated cobalt nanoparticles embedded in nitrogen-doped porous carbon: a bifunctional electrocatalyst for overall water splitting. *Nanoscale Advances* **2019**, *1*, 2293−2302.
(52) Ma, X.; Chang, C.; Zhang, Y.; Niu, P.; Liu, X.; Wang, S.; Li, L. Synthesis of Co-based Prussian Blue Analogues/Dual-Doped Hollow Carbon Microsphere Hybrids as High-Performance Bifunctional Electrocatalysts for Oxygen Evolution and Overall Water Splitting. *ACS Sustainable Chem. Eng.* **2020**, *8*, 8318−8326.
(53) Song, X.; Peng, C.; Fei, H. Enhanced Electrocatalytic Oxygen Evolution by Exfoliation of a Metal−Organic Framework Containing Cationic One-Dimensional $[Co_4(OH)_2]^{6+}$ Chains. *ACS Appl. Energy Mater.* **2018**, *1*, 2446−2451.
(54) Jiang, J.; Huang, L.; Liu, X.; Ai, L. Bioinspired Cobalt-Citrate Metal-Organic Framework as an Efficient Electrocatalyst for Water Oxidation. *ACS Appl. Mater. Interfaces* **2017**, *9*, 7193−7201.
(55) Zhao, T.; Gao, J.; Wu, J.; He, P.; Li, Y.; Yao, J. Highly Active Cobalt/Tungsten Carbide@N-Doped Porous Carbon Nanomaterials Derived from Metal-Organic Frameworks as Bifunctional Catalysts for Overall Water Splitting. *Energy Technol.* **2019**, *7*, 1800969.
(56) Tian, J. W.; Wu, Y. P.; Li, Y. S.; Wei, J. H.; Yi, J. W.; Li, S.; Zhao, J.; Li, D. S. Integration of Semiconductor Oxide and a Microporous (3,10)-Connected Co_6-Based Metal-Organic Framework for Enhanced Oxygen Evolution Reaction. *Inorg. Chem.* **2019**, *58*, 5837−5843.
(57) Wang, X.; Zhang, H.; Yang, Z.; Zhang, C.; Liu, S. Ultrasound-treated metal-organic framework with efficient electrocatalytic oxygen evolution activity. *Ultrason. Sonochem.* **2019**, *59*, 104714.
(58) Liu, X.; Liu, Y.; Fan, L.-Z. MOF-derived $CoSe_2$ microspheres with hollow interiors as high-performance electrocatalysts for the enhanced oxygen evolution reaction. *J. Mater. Chem. A* **2017**, *5*, 15310−15314.
(59) Yang, M.; Zhu, W.; Zhao, R.; Wang, H.; Ye, T.-N.; Liu, Y.; Yan, D. MOF-derived hollow spherical Co_2P@C composite with micro-nanostructure for highly efficient oxygen evolution reaction in alkaline solution. *J. Solid State Chem.* **2020**, *288*, 121456.
(60) Burke, M. S.; Kast, M. G.; Trotochaud, L.; Smith, A. M.; Boettcher, S. W. Cobalt-iron (oxy)hydroxide oxygen evolution electrocatalysts: the role of structure and composition on activity, stability, and mechanism. *J. Am. Chem. Soc.* **2015**, *137*, 3638−3648.
(61) Gong, L.; Chng, X. Y. E.; Du, Y.; Xi, S.; Yeo, B. S. Enhanced Catalysis of the Electrochemical Oxygen Evolution Reaction by Iron(III) Ions Adsorbed on Amorphous Cobalt Oxide. *ACS Catal.* **2018**, *8*, 807−814.
(62) Hao, X.; Jiang, Z.; Zhang, B.; Tian, X.; Song, C.; Wang, L.; Maiyalagan, T.; Hao, X.; Jiang, Z.-J. N-doped carbon nanotubes derived from graphene oxide with embedment of FeCo nanoparticles as bifunctional air electrode for rechargeable liquid and flexible all-solid-state zinc-air batteries. *Adv. Sci.* **2021**, *8*, 2004572.
(63) Deng, X.; Tueysuez, H. Cobalt-Oxide-Based Materials as Water Oxidation Catalyst: Recent Progress and Challenges. *ACS Catal.* **2014**, *4*, 3701−3714.
(64) Okamura, M.; Kondo, M.; Kuga, R.; Kurashige, Y.; Yanai, T.; Hayami, S.; Praneeth, V. K. K.; Yoshida, M.; Yoneda, K.; Kawata, S.; Masaoka, S. A pentanuclear iron catalyst designed for water oxidation. *Nature* **2016**, *530*, 465.
(65) Zhang, M.; de Respinis, M.; Frei, H. Time-resolved observations of water oxidation intermediates on a cobalt oxide nanoparticle catalyst. *Nat. Chem.* **2014**, *6*, 362−367.

https://doi.org/10.1021/acsanm.1c03208
ACS Appl. Nano Mater. 2021, 4, 12663−12671